

Computational Physics II - Exercise 7, Group 14

Wave equation with inhomogeneous propagation velocity in 2 spacial dimensions

Ian LE MEUR Xavier KERVYN

ian.lemeur@epfl.ch xavier.kervyn@epfl.ch

8th May 2021

1 Introduction

This exercise aims to study the equation governing the two-dimensional wave propagation in wave dynamics, which is a second order spatially dependent partial differential equation. This problem will be treated using the centered finite difference method to transform the partial derivatives into a discretized approximation. This will lead to implementing an explicit third level finite difference method, as well as three different boundary conditions: Dirichlet, Neumann and harmonic. Numerically, the points of interest will be the showcase of the behaviour of the simulated wave depending on its initial and boundary conditions, as well as the study of other physical and computational phenomena, such as eigenmodes, stability over time and excitation. Finally, a focus will be given to the study of the waves propagating on an ocean with variable depth.

2 Implementation

We consider the propagation of waves in a two dimensional medium with variable phase velocity $u(x, y)$. The equation that governs the evolution of a perturbation $f(x, y, t)$ is

$$\frac{\partial^2 f}{\partial t^2} = \nabla \cdot (u^2 \nabla f) + a_{ext}(x, y, t), \quad (1)$$

where $a_{ext}(x, y, t) = a_e(x, y) \sin(\omega t)$ is an exterior acceleration with a given spatially-dependent amplitude and frequency. The domain over which the perturbation is considered is a rectangle, $(x, y) \in [0, L_x] \times [0, L_y]$, and the boundary conditions as well as the initial conditions will vary depending on the problem considered. To implement the partial derivatives, a centered finite difference is used:

$$\frac{\partial g}{\partial x}(x_i, y_j, t_n) \approx \frac{g(x_{i+1}, y_j, t_n) - g(x_{i-1}, y_j, t_n)}{2h_x}, \quad (2)$$

$$\frac{\partial^2 g}{\partial x^2}(x_i, y_j, t_n) \approx \frac{g(x_{i+1}, y_j, t_n) - 2g(x_i, y_j, t_n) + g(x_{i-1}, y_j, t_n)}{h_x^2}, \quad (3)$$

with g corresponding to either f or u^2 , and $h_x = x_{i+1} - x_i$ the distance between two points in the discretised regular grid composed of n_x intervals along x and n_y intervals along y . The partial derivatives are defined very similarly with respect to y by replacing h_x by $h_y = y_{j+1} - y_j$, and in the case of time derivatives, h_x or h_y is replaced by $\Delta t = t_{n+1} - t_n$. Implementing these finite differences into equation (1), and denoting $f(x_i, y_j, t_n) \equiv f_{i,j,n}$ yields

$$\begin{aligned} f_{i,j,n+1} &= (\beta_{i,j}^{(x)})^2(f_{i+1,j,n} - 2f_{i,j,n} + f_{i-1,j,n}) + (\beta_{i,j}^{(y)})^2(f_{i,j+1,n} - 2f_{i,j,n} + f_{i,j-1,n}) \\ &\quad + \frac{1}{4} \left[(\beta_{i+1,j}^{(x)})^2 - (\beta_{i-1,j}^{(x)})^2 \right] (f_{i+1,j,n} - f_{i-1,j,n}) + \frac{1}{4} \left[(\beta_{i,j+1}^{(y)})^2 - (\beta_{i,j-1}^{(y)})^2 \right] (f_{i,j-1,n} - f_{i,j+1,n}) \\ &\quad + (\Delta t)^2 a_{ext,i,j,n} + 2f_{i,j,n} - f_{i,j,n-1}, \end{aligned} \quad (4)$$

with $\beta^{(x)}(x, y) = u(x, y)\Delta t/h_x$ and $\beta^{(y)}(x, y) = u(x, y)\Delta t/h_y$. This is referred to as an explicit third level finite difference method, as the perturbation at t_{n+1} can be explicitly solved as a function of the perturbation at t_n and t_{n-1} , thus linking three different time steps together.

Boundary conditions Several different boundary conditions were implemented, the first of which is the homogeneous fixed Dirichlet boundary condition, which when implemented on the left border reads

$$f(0, y, t) = 0 \quad \forall y, t \implies f_{1,j,n+1} = 0 \quad \forall j, n. \quad (5)$$

The next boundary condition is the free Neumann boundary condition, which when implemented on the left border reads

$$\frac{\partial f}{\partial x}(0, y, t) = 0 \quad \forall y, t \implies f_{0,j,n+1} = f_{2,j,n+1} \quad \forall j, n, \quad (6)$$

where $f_{0,j,n+1}$ is an index that is created to maintain a centered finite difference (as in equation (2)). A harmonic boundary condition is also considered, which when implemented on the left border reads

$$f(0, y, t) = A \sin(\omega t) \quad \forall y, t \implies f_{1,j,n+1} = A \sin(\omega t_{n+1}) \quad \forall j, n, \quad (7)$$

with A and ω a given amplitude and frequency. This harmonic condition will sometimes be used as an impulse, in which case the condition will be harmonic for a period or semi-period of oscillation, after which the boundary condition will be changed to either Dirichlet or Neumann, depending on the study. These conditions can similarly be implemented on the other boundaries.

Energy A quantity given by

$$E(t) = \int_0^{L_x} \int_0^{L_y} f^2(x, y, t) dx dy, \quad (8)$$

is to be calculated in the numerical simulation. $E(t)$ is numerically computed using the trapezium method:

$$E(t_n) = \sum_{i,j} \int_{x_i}^{x_{i+1}} \int_{y_j}^{y_{j+1}} f^2(x, y, t_n) dx dy \approx \frac{h_x h_y}{4} \sum_{i,j} (f_{i,j,n}^2 + f_{i+1,j,n}^2 + f_{i,j+1,n}^2 + f_{i+1,j+1,n}^2) \quad (9)$$

where it is important to understand that this quantity is proportional to the energy of the wave at a time t , but is not equal to it: if f has arbitrary units [a.u.], then E has units of $[(\text{a.u.})^2 \text{m}^2]$.

CFL parameter The Courant–Friedrichs–Lewy parameter β_{CFL} is such that

$$\beta_{CFL}^2 = \max(u^2)(\Delta t)^2 \left(\frac{1}{h_x^2} + \frac{1}{h_y^2} \right), \quad (10)$$

where the maximum of $u(x, y)$ is calculated numerically using Newton's method. The stability criterion for the simulation to converge is $\beta_{CFL}^2 \leq 1$, and this will be qualitatively verified further on. Equation (10) was also manipulated to calculate the time step Δt for a given value of β_{CFL} .

3 Numerical simulations

3.1 Constant propagation speed

In this section, we first consider the case of a wave propagating at a constant speed $u = 4$ m/s. The system covers the aforementioned rectangle of dimensions $L_x = 10$ m along the x -axis and $L_y = 6$ m in the y direction.

Reflection at the edges We first analyse the phenomenon of reflection at the boundaries of the rectangle. To simulate this, a sinusoidal impulse of $A \sin(\omega t)$ is initially produced at the left boundary at $x = 0$, with $A = 1$ arbitrary unit and $\omega = 5$ rad/s. The impulse here is generated for half a period of oscillation, such as to obtain only the crest of the sine wave. After a semi period, the left boundary is set to a fixed Dirichlet condition. The system will initially be considered at rest and unperturbed:

$$f(x, y, t \leq 0) = 0 \implies f(x, y, 0) = 0, \quad \frac{\partial f}{\partial t}(x, y, 0) = 0 \quad \forall (x, y). \quad (11)$$

The upper and lower boundaries at $y = 0$ and $y = L_y$, as well as the right boundary at $x = L_x$ are taken to be free Neumann conditions. The wave will thus initially propagate from left to right, be reflected by the Neumann boundary condition on the right boundary, then propagate towards the left, until it is reflected by the Dirichlet boundary condition at the left boundary, at which point it will once again propagate towards the right. Figure 1a shows the propagation of the wave after a time $t = 2$ s since its emission at the left boundary and before it has reached the right boundary of the rectangle. One can identify the sinusoidal wave induced by the harmonic boundary condition. The reflection can be observed in Figure 1b, where a colour plot has been made, showing how the wave propagates along the x axis over time. The (x, y) grid used consists of $n_x = 64$ discrete intervals along the x -axis and $n_y = 64$ intervals along the y -axis. The y axis has not been represented as this problem is purely one dimensional in nature, as can be seen in Figure 1a. Nothing changes along y , and thus each value of the amplitude of the perturbation is taken for a fixed local value of $y = y_{loc}$, with $y_{loc} \approx 0.095$ m. By observing the colour of the line on the plot, one can deduce the amplitude of the wave. Thus, one can observe that with a free

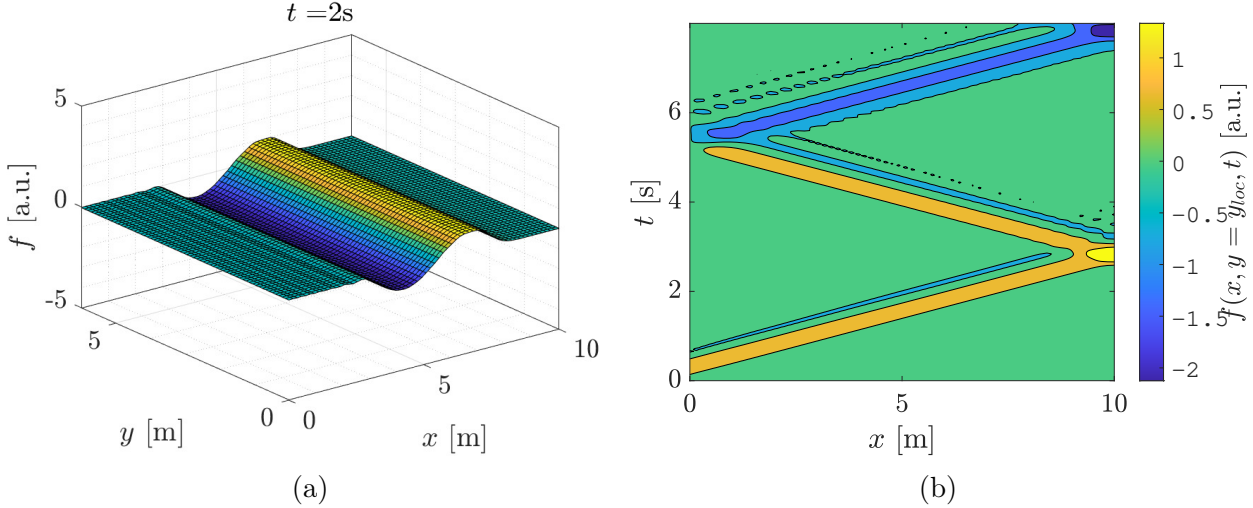


Figure 1: Propagation of the wave for Dirichlet and Neumann boundary conditions at the right boundary. (a) 3D plot of the wave at $t = 2$ s after its emission at the left boundary (harmonic boundary condition); (b) As a function of time and for $y = y_{loc}$.

boundary condition, the sinusoidal wave is reflected in exactly the same manner as it arrived at the boundary, with no phase difference. The amplitude of the wave is the same before and after the reflection. However, in the case of fixed boundary conditions, the reflected wave is reversed; the reflected wave has a phase difference such that the new impulse constitutes a trough instead of a crest (as can be identified by the change in colour after the second reflection). This second reflection quite aptly represents the reflection of a material wave on a taut string, where one end of the string is affixed to a wall. One can also qualitatively affirm that the wave in fact propagates at $u = 4$ m/s, by noticing that the wave makes one return trip from $x = 0$ to $x = L_x$ and back again, covering a distance of $d = 20$ m in approximately $\tau \approx 5$ s.

Eigenmodes We consider the wave equation in two spacial dimensions:

$$\frac{\partial^2 f}{\partial t^2} = u^2 \nabla^2 f, \quad (12)$$

with f our wave function, t denoting time, u the constant propagation speed of the wave, and ∇^2 the two dimensional Laplacian operator. This differential equation is considered on the bounded interval $(x, y) \in [0, L_x] \times [0, L_y]$, along with homogeneous Dirichlet boundary conditions on all four borders, and an initial condition of an eigenmode of vibration. To solve this equation, we proceed by separation of variables:

$$f(x, y, t) = X(x)Y(y)T(t) \implies \frac{\partial^2 f}{\partial t^2} = XYT'' , \quad \nabla^2 f = T(X''Y + XY'') , \quad (13)$$

where the apostrophes denote the derivative operator, and the explicit variable dependence has been omitted to be concise. Re-injecting this Ansatz into equation (12), and dividing by f yields

$$\frac{T''(t)}{T(t)} = u^2 \left(\frac{X''(x)}{X(x)} + \frac{Y''(y)}{Y(y)} \right) = -\omega^2 , \quad (14)$$

with ω a constant, because the left hand side depends only on t , and the right hand side depends only on x and y . To respect the boundary conditions, one finds that the constant in the separation of variables must be strictly negative (which is why we have represented it as $-\omega^2$). We now rearrange equation (14) to obtain

$$\frac{X''(x)}{X(x)} = -\left(\frac{\omega}{u}\right)^2 - \frac{Y''(y)}{Y(y)} = -\kappa^2, \quad (15)$$

with κ a constant as before, by separation of variables. This yields the following boundary value problem for $X(x)$, with the value of X at the boundaries imposed by the homogeneous Dirichlet conditions:

$$X''(x) = -\kappa^2 X(x), \quad X(0) = 0 \quad \text{and} \quad X(L_x) = 0. \quad (16)$$

The general solution to the differential equation is

$$X(x) = C_1 \sin(\kappa x) + C_2 \cos(\kappa x), \quad C_1, C_2 \in \mathbb{R} \quad (17)$$

where the boundary condition at $x = 0$ implies $C_2 = 0$ and the boundary condition at $x = L_x$ reads

$$X(L_x) = C_1 \sin(\kappa L_x) = 0 \implies \kappa = \frac{m\pi}{L_x}, \quad m \in \mathbb{N}, \quad (18)$$

where the negative integer values of m can be absorbed into the constant C_1 , which gives the solution

$$X(x) = C_1 \sin\left(\frac{m\pi}{L_x} x\right), \quad C_1 \in \mathbb{R}, \quad m \in \mathbb{N}. \quad (19)$$

Very similarly, one finds

$$Y(y) = D_1 \sin\left(\frac{n\pi}{L_y} y\right), \quad D_1 \in \mathbb{R}, \quad n \in \mathbb{N}. \quad (20)$$

One can thus define the eigenmodes of vibration as

$$X(x)Y(y) = \hat{f}_{m,n}(x, y) = A \sin\left(\frac{m\pi}{L_x} x\right) \sin\left(\frac{n\pi}{L_y} y\right), \quad m, n \in \mathbb{N} \quad (21)$$

with A a real constant. The corresponding eigenfrequencies $\omega_{m,n}$ can be obtained by substituting (21) into equation (14), one thus obtains

$$\omega_{m,n} = \pi u \sqrt{\left(\frac{m}{L_x}\right)^2 + \left(\frac{n}{L_y}\right)^2}, \quad m, n \in \mathbb{N}. \quad (22)$$

The initial condition for the wave can now mathematically be expressed as

$$f(x, y, t \leq 0) = \hat{f}_{m,n}(x, y) \implies f(x, y, 0) = \hat{f}_{m,n}(x, y), \quad \frac{\partial f}{\partial t}(x, y, 0) = 0 \quad \forall(x, y). \quad (23)$$

Returning to equation (14), and now looking at T , one finds an ordinary differential equation for T , with accompanying initial conditions, i.e. a Cauchy problem:

$$T''(t) = -\omega_{m,n}^2 T(t), \quad T(0) = 1 \quad \text{and} \quad T'(0) = 0 \implies T(t) = \cos(\omega_{m,n} t). \quad (24)$$

It should be noted here that the condition on $T(0)$ is arbitrary, up to a certain non-zero multiplicative coefficient. Here we choose 1, but any other choice could just as well be incorporated into the magnitude of $\hat{f}_{m,n}(x, y)$. The analytic solution for a two-dimensional wave in a rectangle with homogeneous Dirichlet boundary conditions and an initial condition of an eigenmode $\hat{f}_{m,n}(x, y)$ is thus

$$f(x, y, t) = A \sin\left(\frac{m\pi}{L_x}x\right) \sin\left(\frac{n\pi}{L_y}y\right) \cos(\omega_{m,n}t). \quad (25)$$

Numerical verification of the eigenmodes We now aim to simulate the conditions described above to study the eigenmodes of vibration of this system. The simulation is thus executed with Dirichlet conditions on all four boundaries, as well as an initial condition of an eigenmode $\hat{f}_{m,n}(x, y)$ as described above. Here $m = 3, n = 5$ is chosen. The analytic and numerical solutions after a period $T = 2\pi/\omega_{m,n} \approx 0.56$ s are shown in Figure 2a and 2b respectively, where a snapshot at $t = T$ can be observed. One can clearly distinguish the mode $(m, n) = (3, 5)$ in both images. The simulation was conducted with $n_{x,y} = 64$

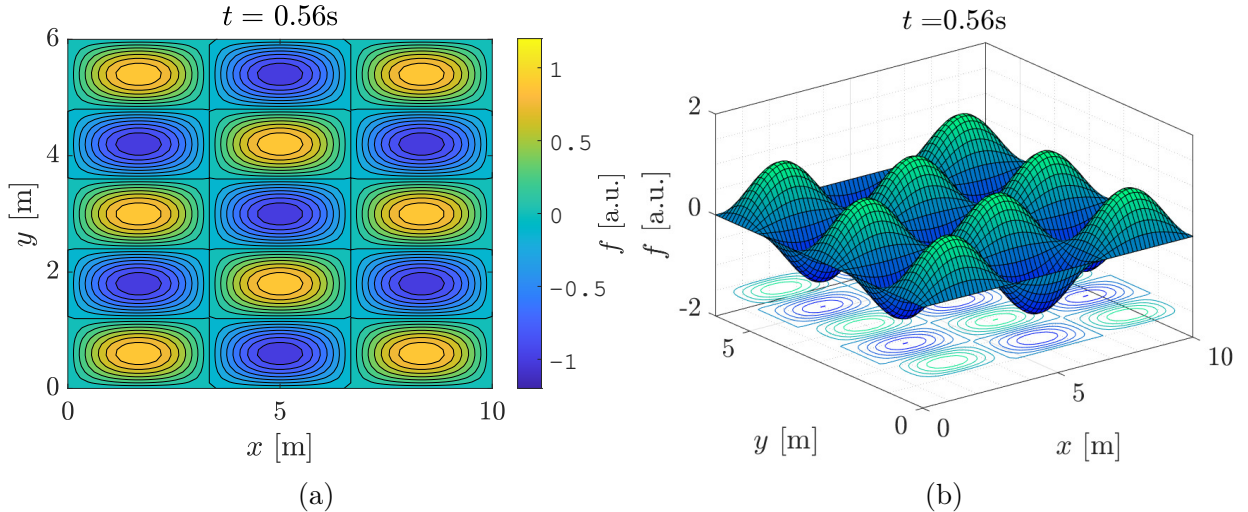


Figure 2: Verification of the eigenmodes after $t = T$. (a) Contour plot of the analytic solution obtained for the eigenmodes. (b) 3D plot of the numerical simulation at $t = T$.

spacial steps in each direction. This seems to qualitatively assess the validity of the analytic solution (25) found for the eigenmodes, as the maximum difference between the analytic and the numerical solution is of about 0.005 arbitrary units.

We now choose to quantitatively study the convergence of the numerical solution. To do this, we execute various simulations with a time step Δt for fixed values of n_x and n_y , and for each simulation we compute the quantity

$$\varepsilon = \left(\int_0^{L_x} \int_0^{L_y} (f_{num}(x, y, t = T) - f_{ana}(x, y, t = T))^2 dx dy \right)^{1/2}, \quad (26)$$

which we will define as our error. We then show how this error varies with β_{CFL} (by varying Δt) on Figure 3a. This was done for three different square (x, y) grids, with $n_{x,y}$ successively equal to 16, 32 and 64. Furthermore, in order to exactly simulate the system during a time

t of an oscillation period T , the time step was defined as $\Delta t = T/N_{steps}$, with N_{steps} taking 30 different integer values in the interval [14, 1000]. Using (10), this procedure yielded each time 30 different values of β_{CFL} , among which only the ones lesser or equal to 1 have been plotted, for stability reasons that will be illustrated in the following paragraph.

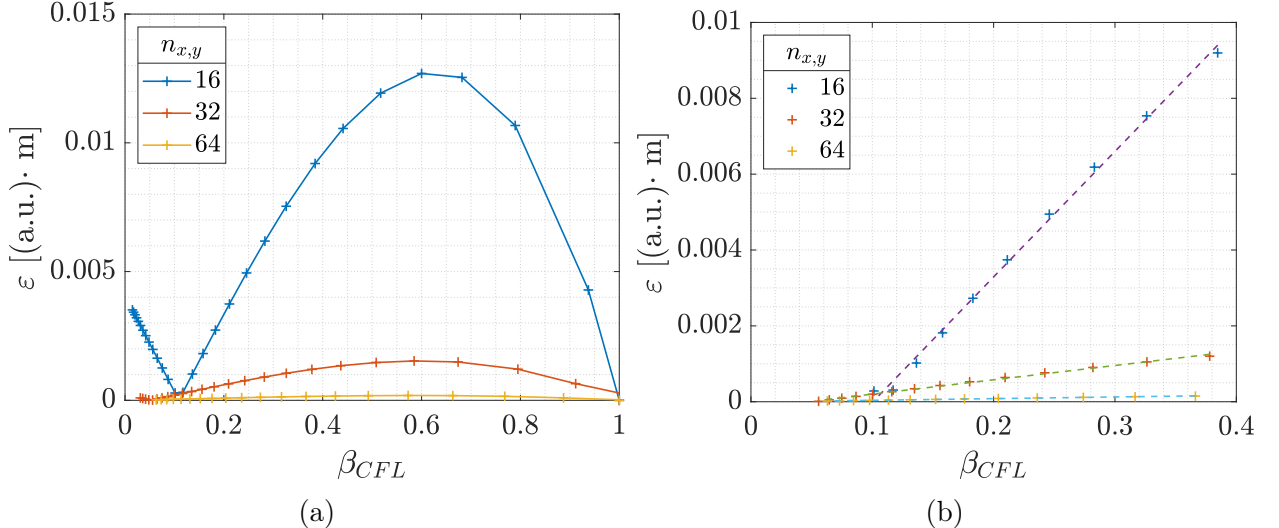


Figure 3: Error ε as a function of the coefficient β_{CFL} (a) For three different mesh grids, over the region $0 \leq \beta_{CFL} \leq 1$. (b) Close-up in the region $0.1 \leq \beta_{CFL} \leq 0.4$ where the data points fit along a line.

One can clearly see that the error ε varies depending on the coefficient β_{CFL} . It reaches a maximum value for $\beta_{CFL} \approx 0.6$ and seems to tend towards zero for $\beta_{CFL} = 0.1$ and $\beta_{CFL} = 1$. It seems that the location of this first minimum depends on the problem considered as well as the spacial discretization. It furthermore appears that the number of spacial intervals inputted to the simulation has a strong impact on the maximum error reached throughout the simulation. As a matter of fact, doubling the number of discrete steps taken in each directions (thus multiplying by four the overall mesh grid) reduced by 88% the maximum error obtained for $n_{x,y} = 16$ and $n_{x,y} = 32$. The same ratio also applies between the plots for $n_{x,y} = 32$ and $n_{x,y} = 64$. This is in concordance with the intuition that augmenting the spacial discretization helps reducing the errors throughout the simulation.

This can be quantitatively illustrated. As a matter of fact, one can identify a range $0.1 \leq \beta_{CFL} \leq 0.4$ where data points seem to be aligned along a line. This is showcased in Figure 3b, where linear best fit lines have been plotted for each data set, in the aforementioned range. Such lines on a graph denote an order of convergence of n , where n is the power on the x data. As ε is plotted as a function of β_{CFL} , this indicates that the order of convergence achieved in this range is of 1. It should be noted that for a method that uses second order centered finite differences, one should expect an order of convergence of 2.

Finally, it can be seen in the graph corresponding to $n_{x,y} = 16$ that the error increases towards an asymptotic value of approximately 0.005 a.u..m as the time steps Δt and thus the parameter β_{CFL} tends to zero. Although this tendency may seem counter intuitive at a first glance, it could be inputted to the resolution of the mesh grid, that could "dominate" for low values of Δt . As matter of fact, this seems to vanish as the spacial resolution is increased.

Limit of stability It is now time to justify the limitation $\beta_{CFL} \leq 1$ made in the previous paragraph. This parameter, defined by (10) in terms of both the spacial and time discrete steps, stands for a stability criterion that governs the convergence of the simulation. Indeed,

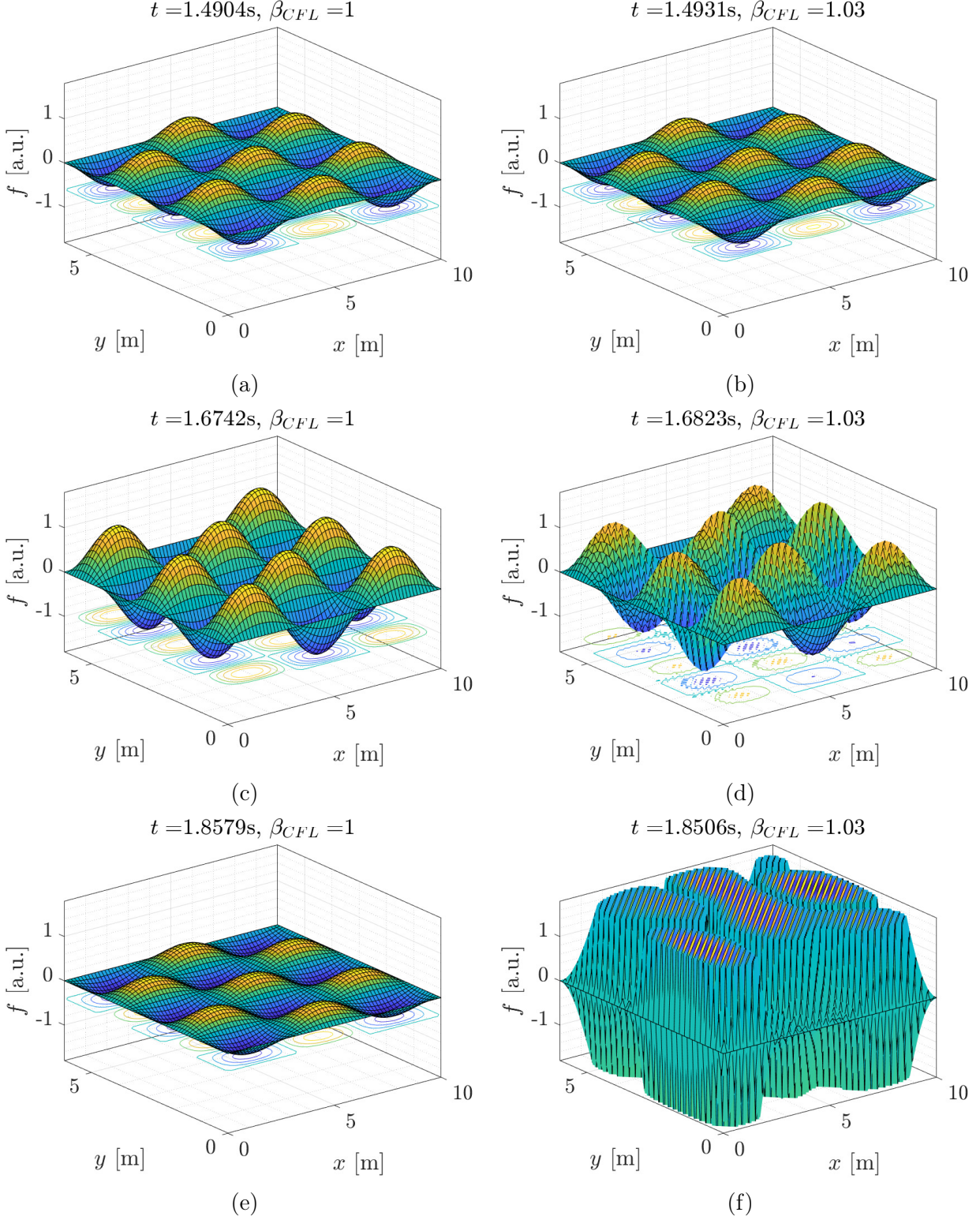


Figure 4: Snapshots of the simulations for $\beta_{CFL} = 1$ and $\beta_{CFL} = 1.03$.

the latter converges only for $\beta_{CFL}^2 \leq 1$, otherwise it diverges exponentially. This was qualitatively verified by conducting numerical simulations with $\beta_{CFL} = 1$ and a slightly larger value of $\beta_{CFL} = 1.03$, with grid parameters $n_{x,y} = 64$, x - and y -modes (3, 5) and over a simulation time $t = 5T$, with T the oscillation period already found while verifying numerically the eigenmodes. The corresponding time steps Δt were computed using (10). Figure 4 gathers three snapshots for each simulation, which were taken approximately at the same time. Figs. 4a, 4c and 4e correspond to the simulation executed with $\beta_{CFL} = 1$, whereas Figs. 4b, 4d and 4f represent the case $\beta_{CFL} = 1.03$. At the beginning of the simulation after a time $t \approx 1.49$ s, one can see on Figs. 4a and 4b that both simulations are still similar, with the same number of modes and same amplitudes.

But 0.2s later, some noticeable differences already appear between the two plots. In Figure 4d, there seems to appear small "peaks" in the all the mesh grids in comparison to Figure 4c, although both plots still have the same overall shape (same modes and amplitudes). The simulation with $\beta_{CFL} = 1.03$ then continues to diverge exponentially from the simulation with $\beta_{CFL} = 1$, and 0.2 s later, one cannot identify any modes, nor see any common characteristic between Figures 4e and 4f. This qualitative comparison thus showcased that a value of β_{CFL} slightly greater than 1 induced an instability of the simulation over time, whereas the case $\beta_{CFL} = 1$ remains stable throughout the simulation.

This is better illustrated in Figure 5, where the wave function is plotted as a function of the physical time t and the coordinate x , for a fixed position $y = y_{loc} \approx 0.09$ m. The simulation was again conducted with $n_{x,y} = 64$ spacial intervals in each direction, over a time $t = 5.5T$ and with a lower value for β_{CFL} of 1.01.

One can again see the peaks that appear at $t > 2$ s within the mesh grid, which is the same phenomenon as the one encountered in Figure 4d. However, this happens slightly later than for the previous case $\beta_{CFL} = 1.03$, which can be explained by the fact that the parameter used is closer to the limit of stability of $\beta_{CFL} = 1$.

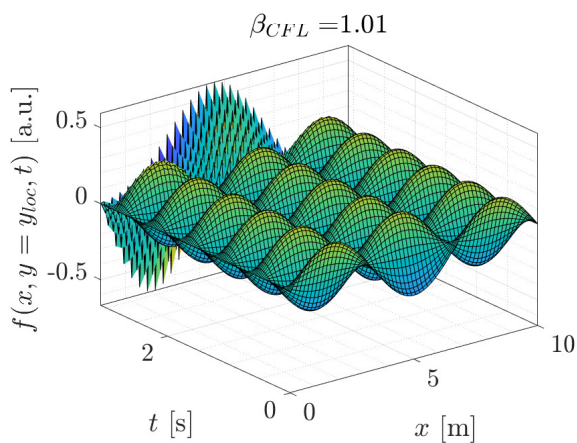


Figure 5: Instability of the simulation. Wave as a function of the time and x -coordinate, with $y = y_{loc}$ and $\beta_{CFL} = 1.01$.

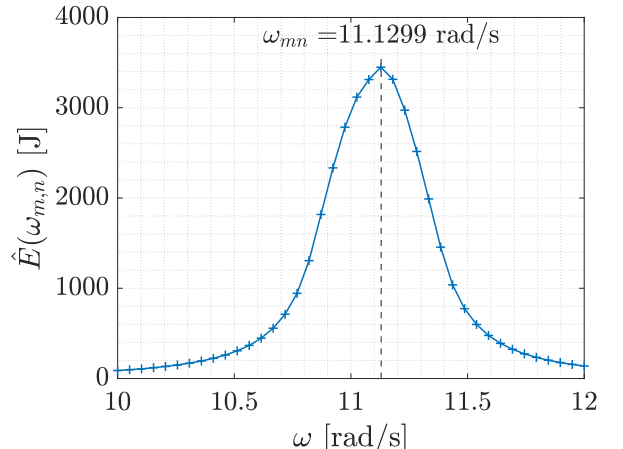


Figure 6: Maximum energy as a function of the angular velocity of the harmonic perturbation for the mode $(m, n) = (3, 5)$.

Resonant excitation of the eigenmodes We now consider a non zero exterior acceleration corresponding to a periodically varied eigenmode: $a_{ext} = \hat{f}_{m,n}(x, y) \sin(\omega t)$, where ω is an arbitrary given frequency. The system is initially unperturbed and at rest. For the mode $(m, n) = (3, 5)$, we have simulated the system over several periods of oscillation of the eigenmode. Several simulations are executed with 40 different values of the angular speed ω in the range [10, 12] rad/s, and for each simulation the quantity

$$\hat{E}(\omega) = \max_t E(t) \quad (27)$$

is recorded. A plot of $\hat{E}(\omega)$ for different values of ω is shown in Figure 6.

One can clearly identify a peak in the maximum energy of the system for acceleration frequencies ω close to the eigenfrequency of the corresponding mode $\omega_{m,n} \approx 11.1299$ rad/s. This thus showcases the existence of a resonance phenomenon for the system when excited at an eigenfrequency. This can be compared to the scenario of a damped harmonic oscillator that is periodically accelerated at a frequency close to the eigenfrequency of the system. In much the same way, for $\omega \approx \omega_{m,n}$, the amplitude of the oscillations of the waves grow enormously. The numerical solution at the end of a simulation over a period of $t_f = 20T$ in the case of this exterior acceleration is then compared with the analytic solution for the eigenmode $\hat{f}_{m,n}(x, y)$. All four boundaries are set to the homogeneous Dirichlet condition. The mesh grid parameters are $n_x = n_y = 64$, the amplitude of the perturbation is of 3 arbitrary units and the time step Δt is defined as $\Delta t = t_f/N_{steps}$, with $N_{steps} = 1000$. The results are qualitatively shown in Figures 7a (showing the analytic solution) and 7b (showing the numerical solution).

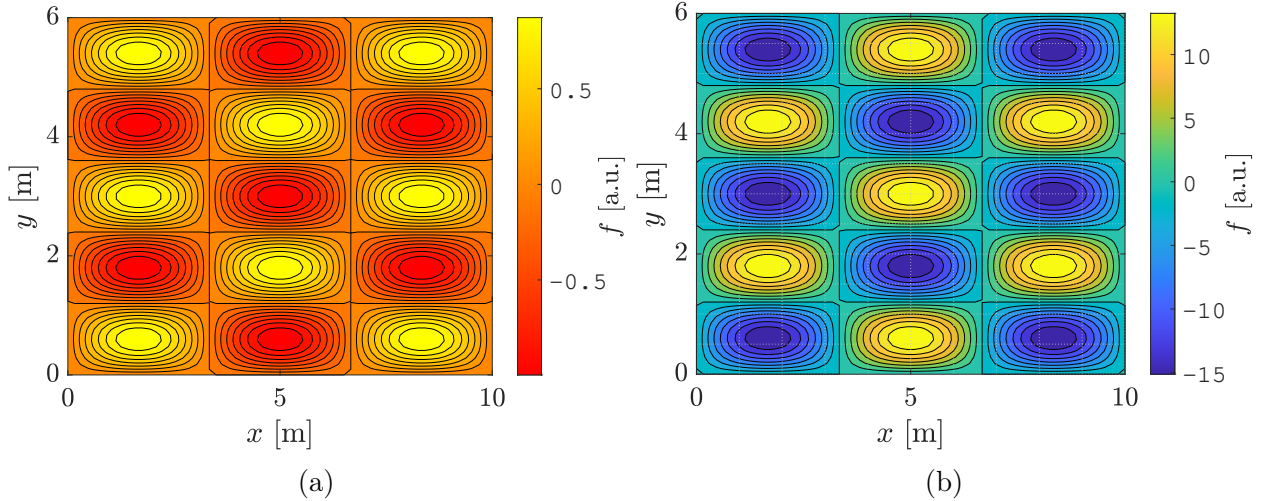


Figure 7: Analytic (a) versus numerical (b) solutions obtained after the simulation.

One can observe that the numerical solution shown strongly resembles the analytic solution, apart from the amplitude of the oscillations. This difference stems from the fact that the amplitude of the acceleration imparted does not have the same units as the units of the wave itself, and thus a certain proportionality factor is to be expected. It should also be noted that the analytic and numerical solution are perfectly out of phase. However, the overall striking resemblance does seem to imply that imparting onto an eigenmode excitation

onto a system that is susceptible to waves tends to coerce the system into producing waves of the same mode and frequency.

3.2 Wave with variable ocean depth

In shallow waters, the propagation speed u of a wave is given by

$$u(x, y) = \sqrt{gh(x, y)}, \quad (28)$$

with $g = 9.81 \text{ m/s}^2$ the gravitational pull and $h(x, y)$ the depth profile. We again consider a rectangle in the (x, y) plane of dimensions $[0, L_x] \times [0, L_y]$ for the simulation. The mesh grid parameters n_x and n_y vary depending on the study and the simulations are executed over a time of $t = 100 \text{ s}$ with a stability parameter of $\beta_{CFL} = 0.95$, which enables one to compute the time step Δt using (10). The boundary conditions implemented consists in a harmonic excitation at the left boundary, that is a sinusoidal wave of amplitude $A = 1 \text{ m}$ and oscillation period $T = 15 \text{ s}$. The three other boundaries are left free (Neumann boundary condition). Two cases for the depth profile shall first be handled in this study. The parameters chosen will be $L_x = 5000 \text{ m}$, $L_y = 2000 \text{ m}$, and constants $h_0 = 1000 \text{ m}$, $h_1 = 20 \text{ m}$, $a = 2000 \text{ m}$ and $b = 5000 \text{ m}$.

Case 1 In this case, the depth profile h is defined as

$$h(x, y) = \begin{cases} h_0 - (h_0 - h_1) \sin\left(\frac{\pi(x-a)}{b-a}\right) & \text{if } a < x < b \\ h_0 & \text{otherwise,} \end{cases} \quad (29)$$

with the constants a , b , h_0 and h_1 defined above. The profile of the corresponding ocean floor, along with a wave of initial amplitude $A = 100 \text{ m}$ (used for scale) is shown in Fig.8.

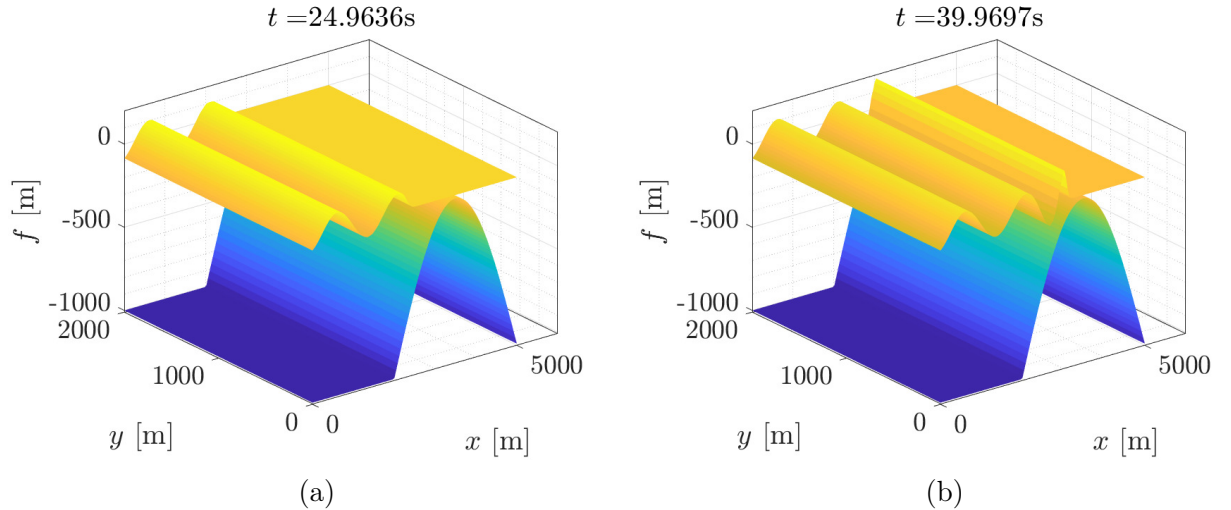


Figure 8: Illustration of the behaviour of the wave with initial amplitude $A = 100 \text{ m}$ (instead of 1 m for scale), along with the ocean depth profile. (a) Propagation of the wave $t \approx 24 \text{ s}$ after emission; (b) Increase in the amplitude and decrease in wavelength of the wave when approaching shallower waters, at $t \approx 40 \text{ s}$ after emission at the left boundary.

From these images, one can note that the amplitude of the wave augments while its wavelength diminishes as the wave approaches shallower waters. To see this more concretely, it helps to notice that this problem is actually only interesting along the x direction (there is no change along y), and thus to plot the evolution of the wave on a colour plot such as the one shown in Figure 9.

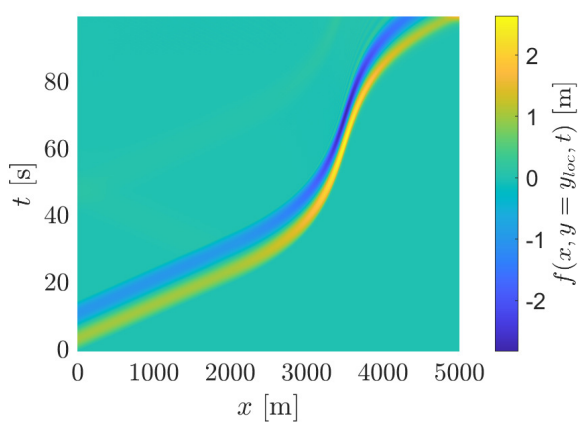


Figure 9: 2D sectional view of the wave as a function of time t and x -coordinate, for a fixed position $y = y_{loc}$. Mesh grid obtained with $n_x = 600$ and $n_y = 4$.

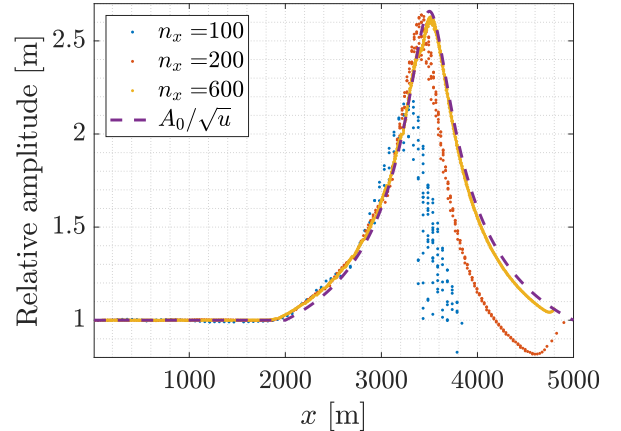


Figure 10: Relative maximum amplitude of the wave along the x -axis over the simulation, for different mesh parameters and compared to the analytic solution.

In this figure, one can observe how a singular wave (created using an impulse) progresses along x . The wave begins at the bottom left, at $x = 0$ and $t = 0$, with an amplitude of 1 m, and first moves at a constant velocity until it reaches $x = a = 2000$ m, where the water starts to become more shallow. At this point, one can observe that the crest begins to rise and the trough begins to deepen (as can be noted by observing the colour, which corresponds to the magnitude of f), until reaching a maximum height of $A_{max} \approx 2.6287$ m in a neighbourhood of $x = 3500$ m, where the ocean is the shallowest. This increase in amplitude is accompanied by a deceleration of the wave, as can be identified by the steepening slope of t versus x , and which is predicted by the wave equation with u given by (28). Finally, the wave seems to decrease in size and gain velocity after having passed the "hill" on the ocean floor.

We now seek to establish how the amplitude of the wave varies over the course of its propagation. In Figure 10, the amplitude of the wave is plotted as a function of x for 3 different simulations with different spatial discretisation. Also shown on the graph is the approximated analytic solution obtained via the WKB method of

$$A(x) = \frac{A_0}{\sqrt{u(x)}} = \left(\frac{h_0}{h(x)} \right)^{1/4}, \quad (30)$$

where the y dependency of both u and h has been omitted in the context of this first case, and where A_0 has been determined using the fact that when $h(x) = h_0$, the amplitude of the wave equals 1 m. It can be noted that as the spacial discretization becomes finer, the numerical solution seems to qualitatively converge towards the approximative analytic solution. The maximum height of the wave predicted by the WKB solution is $A_{max}^{WKB} =$

$A((a + b)/2) = (h_0/h_1)^{1/4} \approx 2.6591$ m, and thus this shows that both the numerical value and the approximated analytic value are quite coherent.

Case 2 In this case, the depth profile h is defined as

$$h(x, y) = \begin{cases} h_0 - (h_0 - h_1) \sin\left(\frac{\pi(x-a)}{b-a}\right) \sin\left(\frac{\pi y}{L_y}\right) & \text{if } a < x < b \\ h_0 & \text{otherwise,} \end{cases} \quad (31)$$

with the constants defined previously. The profile of the corresponding floor is shown in Figure 11.

This time, the y -direction clearly plays a role in the propagation of the wave. This can be seen by again impulsing a single wave as for the case 1 and recording its amplitude over the course of the simulation. 2D snapshots of the amplitude of the wave at four different times during the simulation are gathered in Figure 12. The mesh grid used corresponds to the parameters $n_x = n_y = 256$ and a simulation time of $t_f = 100$ s. The left boundary condition is harmonic, of amplitude $A = 1$ m and oscillation period $T = 15$ s. The stability parameter chosen is again $\beta_{CFL} = 0.95$, which yields a time step $\Delta t \approx 0.06$ s. Only the left boundary is set to harmonic condition, others are left free (Neumann boundary condition).

On Figure 12a, one can see the sinusoidal wave propagating at a time $t \approx 25$ s after its emission. At this stage of the simulation, the wave just reaches the limit of the "flat" floor area, that is to say in the region $x \leq a = 2000$ m in Figure 11. The forefront of the wave indeed seems to be slightly disturbed as the contour lines are not parallel anymore in comparison to the back of the wave (left contours) that still seems to propagate in a flat topography. The amplitude still peaks at its initial value of 1 m as expected.

Figure 12b represents the same impulse approximately 25 seconds later. This time, the wave does not look rectilinear as seen from above, but looks clearly "distorted" by the topography. The wave seems to deepen just before reaching a local maximum amplitude of 4 m, in a very tiny region of the (x, y) plane. The latter corresponds to the peak of the ground profile that can be noted in Figure 11. Moreover, the perturbation forms two "valleys" on both sides of that peak. Otherwise, the amplitude of the overall plane seems to be slightly higher than "initial" level of perturbation, with an amplitude that seems to be slightly greater than 0 (around 0.5 - 1 m).

Twenty-five seconds later, the situation looks completely different. As can be seen in Figure 12c, the amplitudes seem to have been "reversed". Although the overall plane remains at the same level (amplitude between 0 and -1 m), the peak region identified in Figure 12b now presents a recess of amplitude up to -5 m. It still represents a tiny and very localised region of space, but indicates that the emitted wave sort of "bounces" on the peak region and thus its amplitude oscillates in time and stays in the same region of space.

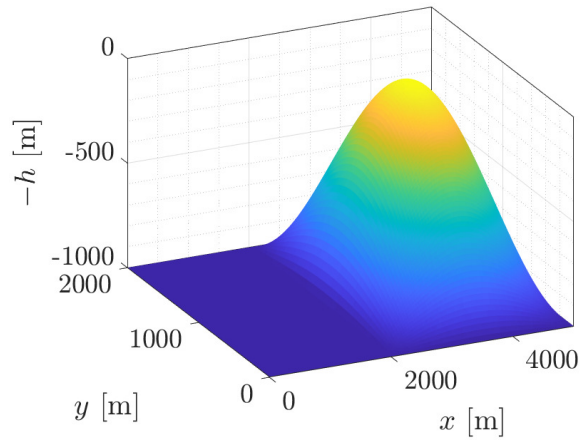


Figure 11: Ocean depth profile for the case 2.

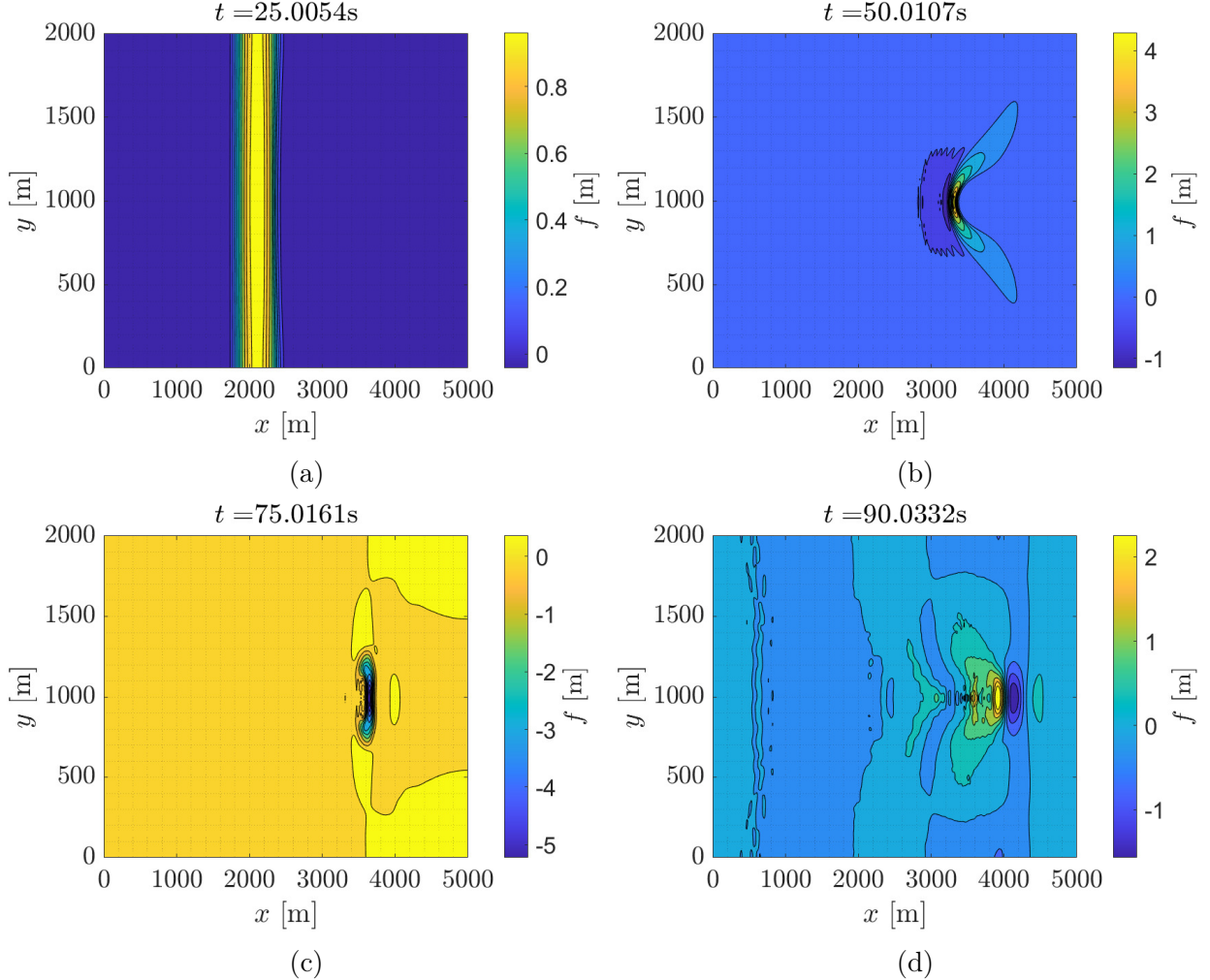


Figure 12: Snapshots of the propagation of the wave in the second case, for a simulation conducted over a time $t_f = 100$ s, with parameters described in the text.

The amplitude still increases over time, reaches an absolute maximum of $A_{max} \approx 8.7938$ m and then decreases as the time approaches end of the simulation. In, figure 12d, which is a snapshot taken approximately ten seconds before the end of the simulation, the amplitude has diminished and the disturbed region has slightly moved to the right. The amplitude now peaks at approximately 2 m and at $x \approx 4000$ m instead of in Figure 12b where it was located at $x \approx 3000$ m.

3.3 Other ocean depth profile

We now consider an ocean floor that rises gradually and linearly, roughly simulating the ocean depth near a land mass, which is thus given by

$$h(x, y) = \begin{cases} \frac{(h_0-h_1)x+ah_1-bh_0}{a-b} & \text{if } a < x < b \\ h_0 & \text{otherwise,} \end{cases} \quad (32)$$

This ocean floor is represented in Figure 13c, and it can be seen that the ocean floor rises from a depth of $h_0 = 5000$ m to a depth of $h_1 = 20$ m in an interval from $a = 1000$ m

to $b = 5000$ m. A sinusoidal impulse of period $T = 5$ s and amplitude $A = 5$ m is then propagated in this system. As can be seen in Figures 13a and 13c, the amplitude of the wave augments and its wavelength diminishes as the water becomes shallower. This explains how and why tsunamis are so dangerous. A relatively small perturbation, at large in waters that are quite deep, travels surprisingly fast (here the wave moves about 3000 m in under 20 s), and quite produce enormous waves when the depth of the ocean reduces close to land. After this point, non-linear phenomena must be used to analyse the circumstances of waves breaking and other factors, but this is a qualitative discussion first and foremost.

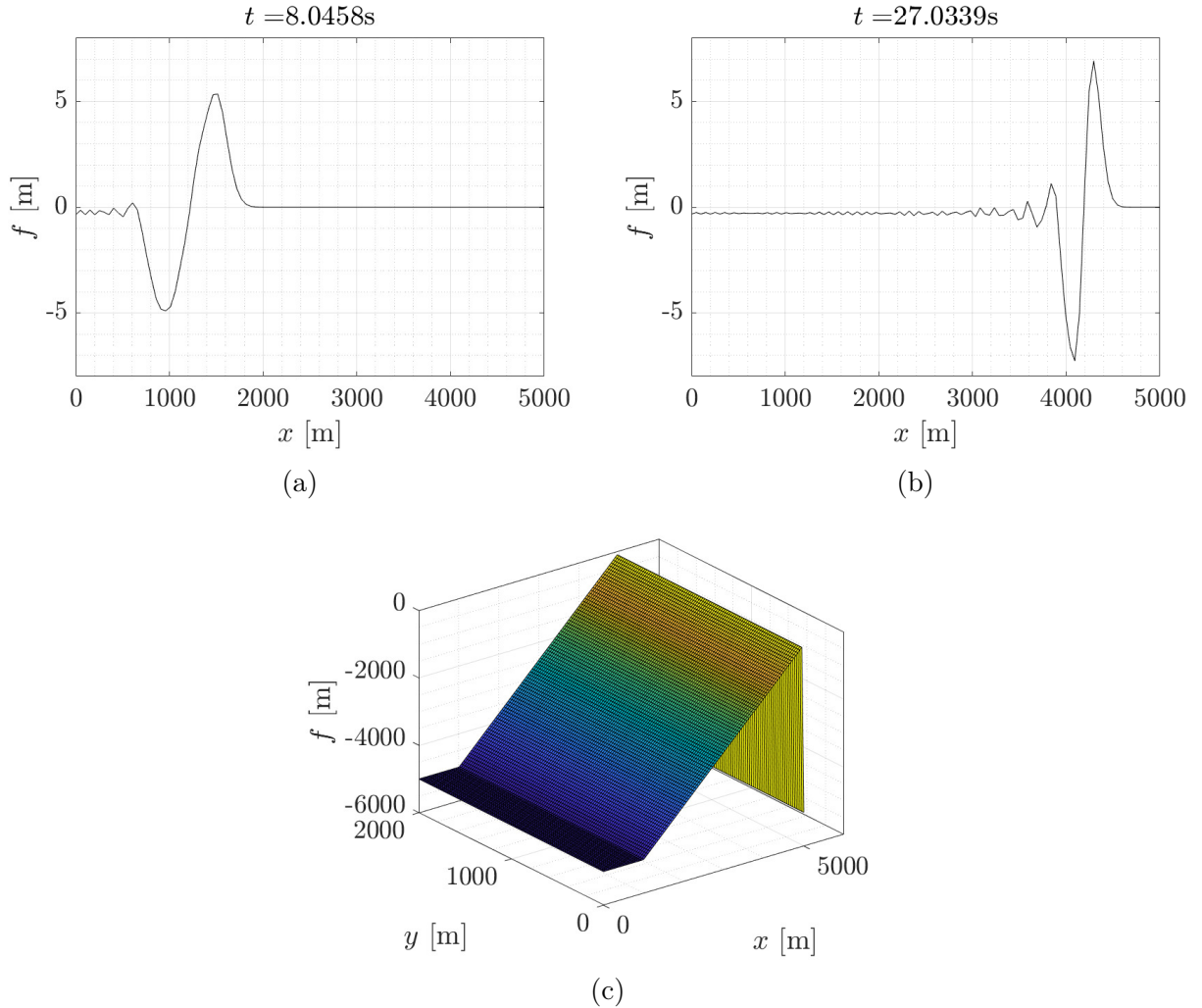


Figure 13: (a) & (b) Snapshots of the propagation of a singular wave impulse approaching a coast line, with parameters given in the text. (c) The ocean floor modelising the depth in a neighbourhood of land, given as a linear function of x .

3.4 New wave equation

In this section, we aim at illustrating what would happen if the wave equation was not given by (1) but rather by

$$\frac{\partial^2 f}{\partial t^2} = u^2 \nabla^2 f + a_{\text{ext}}(x, y, t). \quad (33)$$

This was done by reproducing the analysis conducted for the case 1, with the exact same parameters and ocean depth profile. Two snapshots of the simulation be seen in Figure 14. As the problem does not present any variation along the x -coordinate, it has been chosen to represent a side view along the x -axis only. In Fig.14a, one recognises sinusoidal impulsion

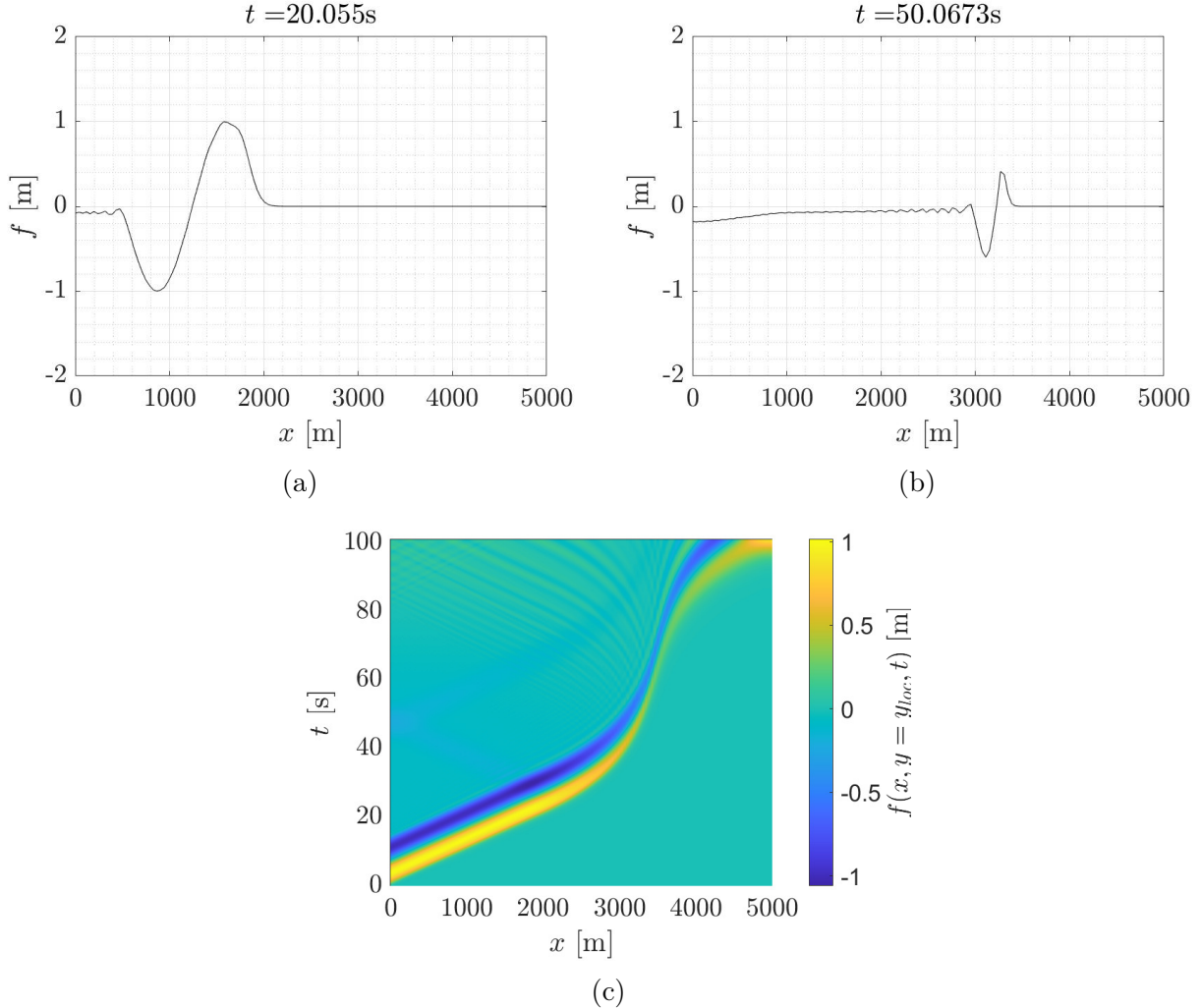


Figure 14: Snapshots of the simulation with the new wave equation and the same parameters as for the case 1. (a & b) Side-views along the x -axis; (c) Color plot of the amplitude as a function of time and the x -coordinate.

at a time $t \approx 20\text{s}$ after its emission. The wave is still in the "flat" ground domain and thus its amplitude is of 1 m, that is to say the initial amplitude inputted. However, the other snapshot presented in Figure 14b of the wave at a time $t \approx 50\text{s}$ shows that this amplitude has significantly diminished over the course of its propagation along the x -axis, having an

amplitude of 0.2 m. It can further be seen on Figure 14c, which is a representation of the amplitude along the x -axis and over the course of the simulation, that the amplitude decreases over time. This is the exact opposite of what had already been seen in Figure 9 as the maximum amplitude is reached at the beginning of the simulation and not at the end. Hence, one can deduce that the physical effect of the new wave equation (33) is to induce a progressive decrease in the amplitude of the emitted wave as it approaches shallower waters, instead of an augment as we have already seen for the case 1.

4 Conclusion

This study has allowed us to study the problem of the wave equation, an essential differential equation which appears in many areas of physics from electrodynamics to acoustics. To tackle this problem numerically, it was important to develop a numerical integration method applicable in two spacial dimensions as well as a temporal dimension, which allowed us to analyse the explicit third level integrator used in this problem. This numerical method was then used to discuss various wave phenomena, such as those of reflection, eigenmodes and resonance, in the case of a constant phase velocity. We then studied the propagation of waves in relatively shallow waters, which is governed by a spatially dependent propagation velocity, in order to discuss the phenomenon which allows for tsunamis. These days, the analysis of such phenomena is carried out in a much more complex manner, taking into account other variables such as the transportation of sedimentation on the ocean floor [1], which allows for hypotheses to be made in order to predict dangerous weather patterns. It could be interesting to derive a differential equation as well as a numerical method that could allow us to envisage such variables.

References

- [1] Daisuke Sugawara, 'Numerical modeling of tsunami: advances and future challenges after the 2011 Tohoku earthquake and tsunami', *Earth-Science Reviews*, Volume 214, 2021, 103498, ISSN 0012-8252, <https://doi.org/10.1016/j.earscirev.2020.103498>. (<https://www.sciencedirect.com/science/article/pii/S0012825220305444>)